A Localised Nano-Resonator Mode in Plasmonic Microcavities

A. Casalis de Pury[1,2], X. Zheng[3], O.S. Ojambati[1], A. Trifonov[4], C. Grosse[1], M-E. Kleemann[1], V. Babenko[2], D. Purdie[2], T. Taniguchi[5], K. Watanabe[5], A. Lombardo[2], G. A. E. Vandenbosch[3], S. Hofmann[2], and J. J. Baumberg*[,1]

[1] Nanophotonics Centre, Cavendish Laboratory, University of Cambridge, JJ Thompson Ave., Cambridge CB3 0HE, UK

[2] Cambridge Graphene Centre and Department of Engineering, University of Cambridge, 9 JJ Thompson Ave., Cambridge CB3 0FA, UK

[3] ESAT-TELEMIC, KU Leuven, B-300, Leuven, Belgium

[4]Spin Optics Lab, Saint Petersburg State University, Saint Petersburg, 198504, Russia

[5]National Institute for Materials Science, 1-1 Namiki, Tsukuba 305-44, Japan

Sub-micron-thick hexagonal boron nitride crystals embedded in noble metals form planar Fabry-Perot half-microcavities. Depositing Au nanoparticles on top of these microcavities forms previously unidentified angle- and polarization-sensitive nano-resonator modes which are tightly laterally confined by the nanoparticle. Comparing dark field scattering with reflection spectroscopies shows plasmonic and Fabry-Perot-like enhancements magnify subtle interference contributions, which lead to unexpected red-shifts in the dark field spectra, explained by the presence of these new modes.

Transparent dielectric materials are employed in diverse micro-optical resonators, ranging from semiconductor heterostructures to van der Waals materials[1-7]. More recently there has been interest in utilising high bandgap materials as part of optoelectronic devices, such as hexagonal boron nitride (hBN), as well as active 2D semiconductors for low-energy switching, such as transition metal dichalcogenides (TMDs)[7-12]. Combining plasmonic metals with such micro resonators introduces rich nano-optics[13-28]. Despite its simplicity and in clear contrast to previous results from related structures [29-32], we find plasmonic scattering processes from Au nanoparticles on sub-micron thick dielectric layers are non-trivial, resulting in two distinct possible sets of nanocavity-nanoparticle modes depending on polarisation and incidence angle. We identify a new mode which, rather than resulting from coupling of Fabry-Perot modes with localised plasmon resonances [27,28], requires angled TM illumination and operates via a different Brewster mode mechanism. For sub-micron thickness dielectric layers, this mode is clearly identified and can be stronger than plasmon-coupled Fabry-Perot modes. The mode is characterised by a nanoscale-confined field which propagates beneath the nanoparticle.

Ultraflat planar microcavities here are formed from high-quality hBN crystals embedded into gold, formed by template-exfoliation (Fig.1, method in SM). Each atomically-flat terrace corresponds to a microcavity of different thickness with simple fabrication giving hundreds of ultraflat planar cavities distributed over cm-scale areas. Monodisperse and near-spherical colloidal Au nanoparticles of 60nm average diameter are then deposited from solution [33]. While our observations apply to all microcavities, hBN is helpfully inert, flat, insulating, chemically robust and lacks exciton resonances that complicate these observations. The resultant samples are broadband illuminated through an objective with numerical aperture NA0.8, so that light is collected for both dark-field (DF) and bright-field (BF) illumination in the angular range 0-53° (Fig.1a). In BF, the angle of incidence and reflection are equal whilst the average DF illumination angle is 58°. Microscope 100x images of a nanoparticle-on-microcavity (NPoMC) sample in BF (Fig.1b) and DF (Fig.1c) resolve individual Au nanoparticles in DF as orange spots on terrace 1 (T1) and green spots on terrace 2 (T2). More than 16 NPs are analysed on each terrace displaying consistent spectra (see SM Fig. 2), while brighter (by $> 3\sigma$) Au NP clusters are excluded, as are NPs near terrace edges.

The observed BF colours result from thin-film interference, which is used to calibrate each terrace thickness from the characteristic Fabry-Perot fringes (Fig.2a), using uniaxial refractive indices $n_{x,y}$=1.65, n_z=2.13 (parallel to the c-axis) [34]. Fitted spectra (dashed) generated by the same generalised Mie solver used to calculate DF scattering (see below), use reflectivities measured from the evaporated Au outside each hBN flake, and give thicknesses L_1=672±10 nm for T1 and L_2=577±8 nm for T2. Minor deviations in fringe amplitude are likely due to differences in Au roughness under and beside each hBN flake.

Dark-field scattering spectra collected from each terrace show intense distinct peaks similar for each nanoparticle (Fig.2b). Solid lines show the average over 22 (T1) and 16 (T2) nanoparticles (dashed lines show standard error). While the scattering efficiency of coupled 60nm Au NPs on bare Si is <0.2%, resonant enhancement here increases the scattered intensity by x18 (T1) and x28 (T2) (Fig.2b). This combination of high intensity and low variability enables reliable identification of features in the spectra such as asymmetric lineshapes and overlapping modes. In particular we note that the scattering peaks are not at the expected positions (dashed lines) from the scattering interference paths depicted in Figure 2(c) and that these peaks shifts differ significantly between the two terraces.

Initially two pathways are considered, interfering the direct back-scattering from the NP with the forward-scattered light after it has propagated multiple times through the underlying microcavity. The phase shift on reflection at the lower hBN/Au interface is $\pi + \delta(E,\theta)$. Dips in BF reflectivity correspond to microcavity resonances, where the resonant optical field inside the hBN increases light absorption in the Au mirror. In this situation the optical field at the top surface is also maximised, so forward scattering from the NP is expected to be strongest at these reflectivity dips (for the same illumination angle). Since DF illumination is recorded at higher incident angles than the BF reflectivity, the cavity resonances blue shift [6,7,34] and for 58° are shown by the vertical dashed lines (Fig.2b). However, this model cannot account for the shifted DF scattering peaks (blue-green arrows, Fig.2b). All scattering peaks from both terraces are red-shifted by different energies from the expected positions based on the simple model above, up to 300meV for the higher energy T2 mode. This suggests that scattering resonances of nanoparticles on micro-cavities are influenced by extra mechanisms besides the outcoupling of planar Fabry-Perot modes.

To better understand the resonant modes in this system, we calculate the extinction spectra without the NP, and scattering spectra with the NP (Fig.3). These are evaluated using a generalized Mie theory (see Supplementary) [35] considering a perfectly spherical Au nano-particle on top of a uniform hBN layer on flat Au (Fig.2c), with the z-axis parallel to the optic axis of the hBN crystal. Initially, the fraction of light entering the hBN is calculated as the incident angle increases. Without the nanoparticle, the interface reflection matrix $\boldsymbol{R}$, which relates the reflected electric field $\boldsymbol{E_r}$ to the incident field $\boldsymbol{E_i}$ with incident s- (E_{is}) and p-polarisation (E_{ip}) via

$$\boldsymbol{E_r} = \boldsymbol{R}\,\boldsymbol{E_i} = \begin{bmatrix} E_{rp} \\ E_{rs} \end{bmatrix} = \begin{bmatrix} R_{pp} & R_{ps} \\ R_{sp} & R_{ss} \end{bmatrix} \begin{bmatrix} E_{ip} \\ E_{is} \end{bmatrix} \tag{1}$$

is diagonal (R_{ps}=R_{sp}=0), leaving only $R_{pp} = R_{TM}$ and $R_{ss} = R_{TE}$. Defining incident and reflected electric fields in terms of polarisation-dependent refractive indices and incident angle θ_i, the overall TM reflection coefficient r_{TM} is described by [6,36]

$$r_{TM} = \frac{n_{xy} n_z \cos(\theta_i) - [{n_z}^2 - \sin^2(\theta_i)]^{1/2}}{n_{xy} n_z \cos(\theta_i) + [{n_z}^2 - \sin^2(\theta_i)]^{1/2}} \tag{2}$$

(assuming air above) and similarly for TE. The TE reflection resonances are equally-spaced at normal incidence and blue shift together with angle (Fig.3a). For TM reflectivity (Fig.3b), this picture is complicated by effects at Brewster's angle (white dashed Fig.3) where the reflection at the air-hBN surface vanishes, eliminating multiple interference. Beyond this angle,

$$\theta_B = \operatorname{asin}\left(\left[\frac{{n_{xy}}^2 - 1}{{n_{xy}}^2 - {n_z}^{-2}} \right]^{1/2} \right) \simeq 56° \tag{3}$$

the phase on reflection reverses, shifting the resonances by half their spacing.

This generalised Mie model shows scattering from the NP atop the microcavity is indeed enhanced at each extinction maxima (Fig.3c,d). TE scattering peaks blue-shift with angles matching the reflectivity dips, weakening slightly at θ_B when polarisation-flipped NP scattering disappears. The predicted TE scattering peaks at 58° match the observed peaks at 2.25eV and 1.55eV (Fig.3b) to within 0.1eV. The larger extinctions at higher energy come from the stronger interband Au absorption above 2.5eV.

By constrast, a completely different predicted behaviour is seen for TM polarised scattering (Fig.3d). Although blue-shifts are initially seen, a set of new modes appears around θ_B, which dominate the total (TE+TM) scattering at 58°. Since scattering measurements are typically taken at high angles $\sim \theta_B$, it is vital to understand the origin of these NPoMC modes.

Comparing TM extinction (Fig.3b) to scattering (Fig.3d) highlights these peculiarities. At θ_B, the extinction shows no microcavity modes, however the scattering spectrum gives new sharp modes. In simulations of the thinner microcavity T2 (Fig.3e,f), the new peak at 1.9eV becomes the dominant cavity mode, with a 200meV red-shift from the expected position of the TE scattering peak (Fig. 3e, blue-green arrow). This combination of nano-resonator and Fabry-Perot modes accounts well for the bright mode near 1.8eV in Fig. 2(b).

The theory shows these modes are produced by back-scattering from the NP, creating transverse localised cavity modes underneath it which are spatially confined in-plane to the nanoscale geometry of the NP (Fig.4). Even for illumination angles significantly less than θ_B these surface modes can be excited and out-coupled. This new nano-resonator mode (NRM) is only seen at energies that can excite the microcavity-coupled vertical dipole antenna, forming a new scattering resonance at 2.25eV.

To explore the nano-resonator modes, we track how they vary with increasing microcavity thickness (Fig.4a) [6,7,36]. The NRMs redshift with increasing hBN thickness for constant illumination angle of 58°. Above L=300nm, several modes are seen, with energy spacings which decrease as expected for Fabry-Perot-type modes. Between the strongly-excited NRMs are weaker resonances matching the normal TE microcavity modes. Plotting the thickness-dependent Q-factor of the dispersive NRMs shows a periodic modulation under an increasing envelope (Fig.4b).

These resonant modes can be excited at incident angles from 40-80° with energies from 1.4-2.4eV. The high-angle resonant lowest mode is clearly visible for hBN L>90nm (Fig.4c,d). They appear strongest when near-resonant with the nanoparticle transverse plasmon mode around λ=550nm. The angle of maximum scattering intensity (blue and green lines, Fig.4c,d) shifts from 52° to 68° when the hBN thickness increases from 90 to 130nm, showing their coupling is not precisely tied to θ_B.

At thicknesses of 80-170nm the lowest NRM has least extra contribution from the FP-coupled modes (Fig.4a). Experimentally, nanoparticles on hBN flakes within this range display ring-shaped dark-field scattering images due to the high-angle outcoupling of light from the NRMs (Fig. 4e). This confirms their dominant out-of-plane E_z resonant fields, completely different from Fabry-Perot microcavities. These TM nano-resonator modes seen in the NPoMC geometry are thus attributed to multiple scattering and reflection underneath the NP (Fig.4f). This is because at θ_B all other cavity feedback disappears at the hBN/air interface. Treating scattering from the nanoparticle as a microcavity end mirror with low reflectivity (following Fabry-Perot behaviour), we indeed expect the Q-factor to increase with thickness. Such nano-resonators approach the limiting case when the lateral dimensions of a cavity back-reflector approach a point. As expected, the Q-factor per unit length decreases with increasing thickness since diffraction from NP causes lateral spreading of the retro-reflecting light beyond the optical cross-section of the resonant NP (see SM Fig. 4). The NRM field distribution (Fig.4f) is similar to that from individual Au NPs, but resonant at 58° and nearly 10-fold stronger than without the underlying Au mirror (see SM Fig. 5).

The NRMs depend on cavity thickness as for conventional Fabry-Perot modes, but experience far stronger plasmonic phase shifts due to multiple scattering, which needs to be taken into account. Plasmonically enhanced cross-sections mean that although dielectric nanoparticles also show NRMs,

they are more than fifty-fold weaker (SM Fig. 6). NRM modes are excited in all such plasmonic NP-dielectric microcavities, even with lower refractive indices (such as SiO_2, see SM Fig. 7), thus demonstrating the universal nature of the modes in plasmonic-microcavity heterostructures.

These nano-resonator modes resemble previously observed 'Brewster modes', but with the Bragg mirror replaced by flat Au and a NP. Such modes follow the condition [37,38]

$$E = \frac{hc^2}{2nL}\left(p + \frac{1}{2}\right)\cos(\theta) \tag{4}$$

where p is an integer, arising from additional π phase jumps compared to Fabry-Perot modes. Here, nano-resonator modes experience additional shifts of $\delta(E,\theta)$ dependent on the mirror, cavity and nanoparticle compositions, with some analogy to Goos-Hänchen effects. This shifts the peaks considerably away from Eqn.(4). As a result, these NRMs critically probe the morphology and scattering at the top interface.

Although our calculations yield good agreement with the mode energies, they do not account well for measured scattering intensities. Our model predicts modes at energies close to the transverse plasmon mode should have greatest scattering intensity, but experimentally the modes at lower energies are much stronger. We suggest this may be due to additional Fano resonance [11,12] from the continuum scattering background (due to the slightly rough lower Au surface, grey line Fig.2b), which is stronger at lower energies. Such Fano effects produce the asymmetric-lineshape low-energy peaks and also the small (50 meV) extra blue-shifts of the calculated modes (grey points, Fig.2b) compared to those experimentally observed. It is also possible that the morphology of the nanoparticle favours outcoupling of cavity modes at lower energies.

In conclusion, we embed exfoliated hBN crystals in Au forming uniform planar half-microcavities. By depositing Au nanoparticles on top of these crystals to form NP-on-microcavity (NPoMC) structures and using single nanoparticle spectroscopy, we probe plasmonic and Fabry-Perot enhancements identifying interfacial scattering mechanisms which control red-shifts in the mode positions. We identify a new microcavity nano-resonator mode which can be excited only for TM polarisation at angles $\theta_B \pm 20°$ and which depends on microcavity length and refractive index. We show that this mode arises from multiple reflections between scatterer and Au mirror. Subtle phase shifts and Fano coupling within this microcavity control its exact spectral position. These NRM modes are vital to understand when exploring the coupling of nanoparticles with the new materials landscape of TMDs. The same fabrication techniques can be used to produce NPoMC structures with other TMDs instead of hBN. This work is valuable in studying architectures (such as semiconductor and dielectric microcavities) which take advantage of enhancements at nanostructure- or NPoMC-interfaces. Moreover, due to the extreme sensitivity of these modes, they are suitable for exploring novel angle- and polarization-sensitive optical devices that are integrable and easy to fabricate.

This work is supported by EPSRC grants EP/N016920/1, EP/L027151/1, and NanoDTC EP/L015978/1, and EU Horizon 2020 grant 785219. O.S.O. acknowledges Rubicon fellowship from the Netherlands Organisation for Scientific Research.

* jjb12@cam.ac.uk

Figures:

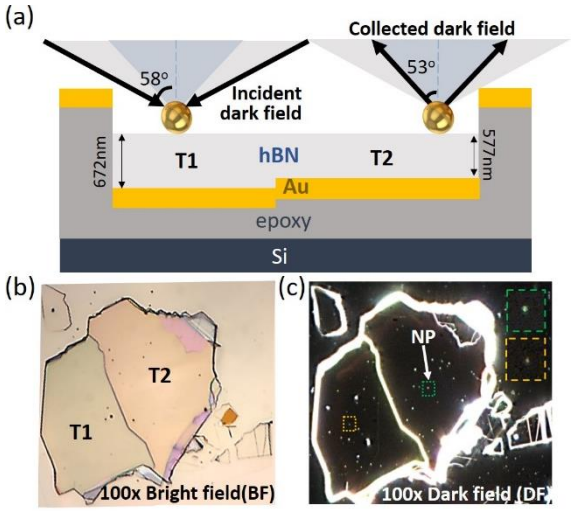

FIG. 1. Embedded hBN sample ~60µm wide, with two crystal terraces (T1,T2). (a) Cross-section after nanoparticle deposition, showing in-/out-coupling angles for illumination with 0.8NA objective. (b) Bright-field and (c) dark-field images at 100x magnification showing individual nanoparticles on each terrace.

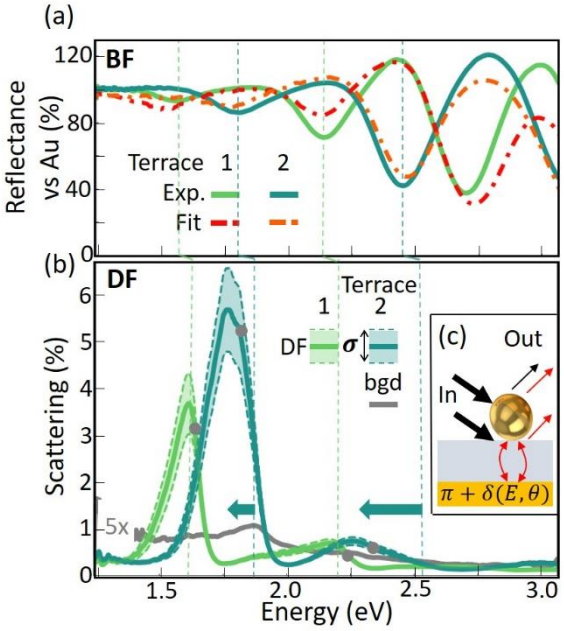

FIG. 2. (a) Bright-field reflectance, and (b) dark-field scattering from 22 (T1) and 16 (T2) nanoparticles. Dashed lines show one standard error bound, grey line is scattering background (x5) from lower hBN/Au interface away from NPs, grey dots mark peak positions of Fano resonances from resulting interference. Vertical lines show expected TE-polarised wavelengths for $L_{1,2}$. (c) Schematic interference in scattering.

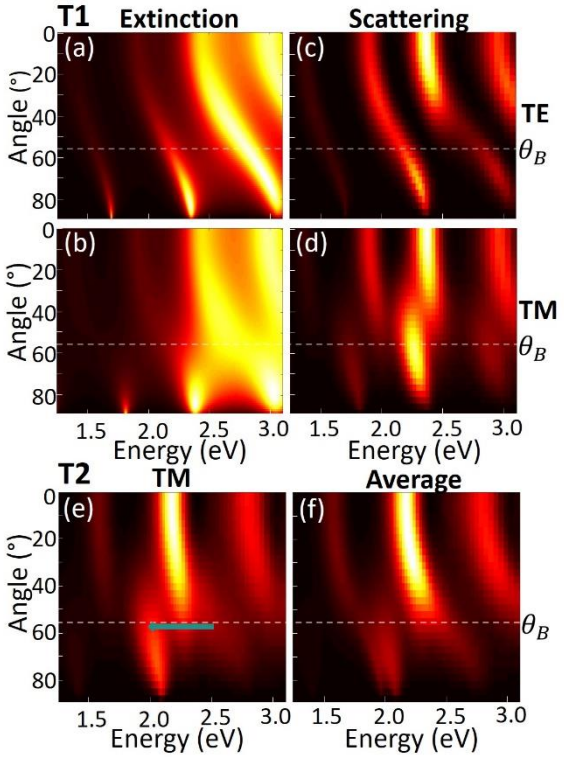

FIG. 3. Generalised Mie calculations for T1 (a-d) and T2 (e,f). For T1, extinction without NP (a,b) and scattering spectra for NP-on-microcavity (c,d) are shown as angle increases. Brewster angle $\boldsymbol{\theta_B}$ is dashed. Extinction is from 0% (black) to 100% (white), scattering from 0% (black) to 5% (white). For T2, calculations are for (e) TM scattering and (f) average of TE and TM scattering. Blue arrow is comparison with Fig 2.

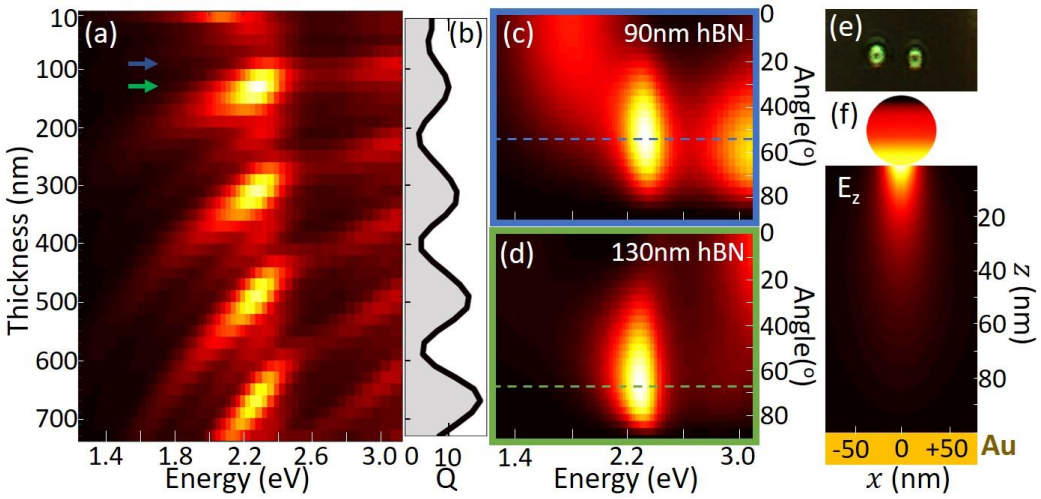

FIG. 4. (a) Thickness dependence of TM scattering of nano-resonator modes at $\boldsymbol{\theta_i}$= $\boldsymbol{\theta_B}$=58°, and (b) Q-factors. Arrows mark $\boldsymbol{L}$=90,130nm for angle-dependences in (c,d) where dashed lines mark angle of maximum scattering. (e) Typical experimental DF scattering images of 80-130nm thick hBN nano-resonators at 100x magnification. (f) Field map of surface charges on outside of 60nm nanoparticle, and scattered electric field ($\boldsymbol{E_z}$) inside hBN for nano-resonator mode with $\boldsymbol{L}$=110nm, $\boldsymbol{\theta_i}$=58°.

[1] C. Jin *et al.*, Nature Physics 13, 127 (2017).

[2] S. Latini, K. T. Winther, T. Olsen, and K. S. Thygesen, Nano Letters 17, 938 (2017).

[3] G. H. Lee, Y. J. Yu, C. Lee, C. Dean, K. L. Shepard, P. Kim, and J. Hone, Applied Physics Letters 99, 1 (2011).

[4] S. Dai *et al.*, Nature Nanotechnology 10, 682 (2015).

[5] Q. Wang *et al.*, Nano Lett 17, 7593 (2017).

[6] Alexey Kavokin, J.J. Baumberg, Guillame Malpuech, Fabrice P. Laussy, *Microcavities* (Oxford University Press, 2017).

[7] Vahala, K., *Optical microcavities*, Nature, 424, 839–846 (2003).

[8] X. Liu, T. Galfsky, Z. Sun, F. Xia, E.-c. Lin, Y.-H. Lee, S. Kéna-Cohen, and V. M. Menon, Nature Photonics 9, 30 (2014).

[9] S. Dufferwiel *et al.*, Nat Commun 6, 8579 (2015).

[10] L. C. Flatten, Z. He, D. M. Coles, A. A. Trichet, A. W. Powell, R. A. Taylor, J. H. Warner, and J. M. Smith, Sci Rep 6, 33134 (2016).

[11] H. Y. Jeong *et al.*, ACS Nano 10, 8192 (2016).

[12] W. Wang, A. Klots, Y. Yang, W. Li, I. I. Kravchenko, D. P. Briggs, K. I. Bolotin, and J. Valentine, Applied Physics Letters 106 (2015).

[13] M. E. Kleemann *et al.*, Nature Communications 8 (2017).

[14] J. Mertens *et al.*, Nano Letters 13, 5033 (2013).

[15] D. O. Sigle *et al.*, ACS Nano 9, 825 (2015).

[16] T. Low *et al.*, Nature Materials 16, 182 (2017).

[17] D. Zheng, S. Zhang, Q. Deng, M. Kang, P. Nordlander, and H. Xu, Nano Letters 17, 3809 (2017).

[18] S. Butun, S. Tongay, and K. Aydin, Nano Letters 15, 2700 (2015).

[19] S. Najmaei, A. Mlayah, A. Arbouet, C. Girard, J. Léotin, and J. Lou, ACS Nano 8, 12682 (2014).

[20] W. Liu, B. Lee, C. H. Naylor, H. S. Ee, J. Park, A. T. C. Johnson, and R. Agarwal, Nano Letters 16, 1262 (2016).

[21] J. Wen *et al.*, Nano Lett 17, 4689 (2017).

[22] N. Lundt *et al.*, Nat Commun 7, 13328 (2016).

[23] R. Chikkaraddy *et al.*, ACS Photonics 4, 469 (2017).

[24] X. Zheng, N. Verellen, V. Volskiy, V. K. Valev, J. J. Baumberg, G. A. E. Vandenbosch, and V. V. Moshchalkov, Optics Express 21, 31105 (2013).

[25] C. Tserkezis, R. Esteban, D. O. Sigle, J. Mertens, L. O. Herrmann, J. J. Baumberg, and J. Aizpurua, Physical Review A - Atomic, Molecular, and Optical Physics 92, 1 (2015).

[26] F. Benz, B. de Nijs, C. Tserkezis, R. Chikkaraddy, D. O. Sigle, L. Pukenas, S. D. Evans, J. Aizpurua, and J. J. Baumberg, Optics Express 23, 33255 (2015).

[27] M. E. Kleemann *et al.*, ACS Nano 11, 850 (2017).

[28] Z. Xi, Y. Lu, W. Yu, P. Yao, P. Wang, and H. Ming, Opt Lett 38, 1591 (2013).

[29] H. H. Anirban Mitra, Stefano Palomba, and Lukas Novotny, Optics Letters 35, 953 (2010).

[30] M. A. Schmidt, D. Y. Lei, L. Wondraczek, V. Nazabal, and S. A. Maier, Nat Commun 3, 1108 (2012).

[31] S. D.-G. Mohsen Bahramipanah, Banafsheh Abasahl, and Olivier J. F. Martin, ACS Nano 9, 7 (2015).

[32] J. Li, M. Jiang, C. Xu, Y. Wang, Y. Lin, J. Lu, and Z. Shi, Sci Rep 5, 9263 (2015).

[33] M. R. Hauwiller, L. B. Frechette, M. R. Jones, J. C. Ondry, G. M. Rotskoff, P. Geissler, and A. P. Alivisatos, Nano Lett 18, 5731 (2018).

[34] T. I. a. T. Sato, Journal of Crystal Growth 1, 689 (1983).

[35] X. Zheng, A. Casalis de Pury, R. Mittra, J. J. Baumberg, and G. A. E. Vandenbosch, IEEE Transactions on Antennas and Propagation (2019), submitted

[36] R. M. A. Azzam and N. M. Bashara, *Ellipsometry and polarized light* (North-Holland Pub. Co., 1977).

[37] H. F. Mahlein, J. Opt. Soc. Am. 64, 647 (1974).

[38] T. Taliercio, V. N. Guilengui, L. Cerutti, E. Tournié, and J.-J. Greffet, Optics Express 22, 24294 (2014).